Achieving Tunable High-Performance Giant Magnetocaloric Effect in Hexagonal Mn-Fe-P-Si Materials through Different D-Block Doping

Zhang, Fengqi; Kiecana, Anika; Wu, Ziying; Bai, Zhaowen; Chen, Huaican; Yan, Xun Wang; Ma, Fengjie; Dijk, Niels van; Brück, Ekkes; Ren, Yang

DOI
10.1002/adfm.202409270

Publication date
2024

Document Version
Final published version

Published in
Advanced Functional Materials

ADVANCED FUNCTIONAL MATERIALS
www.afm-journal.de

Achieving Tunable High-Performance Giant Magnetocaloric Effect in Hexagonal Mn-Fe-P-Si Materials through Different *D*-Block Doping

Fengqi Zhang, Panjun Feng, Anika Kiecana, Ziying Wu, Zhaowen Bai, Wenjie Li, Huaican Chen, Wen Yin, Xun-Wang Yan, Fengjie Ma,* Niels van Dijk, Ekkes Brück, and Yang Ren**

Compared with traditional techniques, solid-state magnetocaloric phase transition materials (MPTMs), based on the giant magnetocaloric effect (GMCE), can achieve a higher energy conversion efficiency for caloric applications. As one of the most promising MPTMs, the hexagonal $(Mn,Fe)_2(P,Si)$-based compounds host some advantages, but the existing hysteresis and relatively unstable GMCE properties need to be properly tackled. In this study, it is found that substitutions with Ni, Pd, and Pt can maintain and even enhance the GMCE (≈8.7% maximum improvement of $|\Delta s_m|$). For a magnetic field change of $\Delta\mu_0 H = 2$ T, all samples obtain a $|\Delta s_m|$ in the range of 20–25 J kg^{-1} K^{-1} with a low thermal hysteresis ΔT_{hys} (≤5.6 K). The performance surpasses almost all other $(Mn,Fe)_2(P,Si)$-based materials with ΔT_{hys} (<10 K) reported until now. The occupancy of substitutional Ni/Pd/Pt atoms is determined by X-ray diffraction, neutron diffraction, and density functional theory calculations. The difference in GMCE properties upon doping is understood from the competition between a weakening of the magnetic exchange interactions and the different degrees of orbital hybridization among 3*d*-4*d*-5*d* elements. The studies elaborate on the responsible mechanism and provide a general strategy through *d*-block doping to further optimize the GMCE of this materials family.

1. Introduction

Worldwide greenhouse gas emissions have led to serious problems like global warming and climate change, which heavily threaten human society and require urgent action to reduce it. One of the most promising ways is to improve the energy efficiency of engines by lowering their energy input.[1] Currently, the main energy conversion technology for cooling and heating (20%–30% of total energy utilization) is the widely used vapor-compression technique among heating-ventilation air-conditioning (HVAC) fields. The technique however always has a limited energy efficiency, which requires to be upgraded. Developing a wide array of cooling strategies is vital for our eco-sustainable society.[2] An efficient alternative approach involves the use of versatile solid-state phase transition caloric effects for this purpose. Within these, the magnetocaloric energy conversion ($M_{CE}EC$) on the basis of magnetocaloric

F. Zhang, Z. Bai, W. Li, Y. Ren
Department of Physics
City University of Hong Kong
Kowloon, Hong Kong SAR 999077, China
E-mail: f.zhang-7@tudelft.nl; yangren@cityu.edu.hk

F. Zhang, A. Kiecana, Z. Wu, N. van Dijk, E. Brück
Fundamental Aspects of Materials and Energy (FAME)
Faculty of Applied Sciences
Delft University of Technology
Mekelweg 15, Delft 2629JB, The Netherlands

The ORCID identification number(s) for the author(s) of this article can be found under https://doi.org/10.1002/adfm.202409270

DOI: 10.1002/adfm.202409270

P. Feng, F. Ma
The Center for Advanced Quantum Studies and School of Physics and Astronomy
Beijing Normal University
Beijing 100875, China
E-mail: fengjie.ma@bnu.edu.cn

P. Feng, F. Ma
Key Laboratory of Multiscale Spin Physics (Ministry of Education)
Beijing Normal University
Beijing 100875, China

H. Chen, W. Yin
Spallation Neutron Source Science Center
Dalang, Dongguan 523803, China

H. Chen, W. Yin
Institute of High Energy Physics
Chinese Academy of Sciences
Beijing 100049, China

X.-W. Yan
College of Physics and Engineering
Qufu Normal University
Qufu, Shandong 273165, China

effect (MCE) has the highest possibility to reach commercialization.[3,4] It can attain a substantially improved energy efficiency of more than 60%, and as an emerging sustainable technique, the $M_{CE}EC$ is environmentally friendly with no hazardous refrigerants (like hydrofluorocarbons) and no noise production during cycling.

The foundation of the $M_{CE}EC$ is the giant magnetocaloric effect (GMCE), accompanied by an isothermal magnetic entropy change (Δs_m) and an adiabatic temperature change (ΔT_{ad}) when the solid-state phase transition takes place.[5,6] In the last two decades, numerous first-order magnetic transition (FOMT) magnetocaloric materials (MCMs) that demonstrate a GMCE have sprung up, including $Gd_5(Si_2Ge_2)$,[7] $(Mn,Fe)_2(P,X)$-based compounds (X = As, Ge, Si),[8] $La(Fe,Si)_{13}$-based materials,[9] Ni-Mn-X based magnetic Heusler alloys (X = Ga, In, Sn, Sb, (Co)Ti),[10,11] FeRh,[12] and Mn-M-X (M = Co, Ni and X = Si, Ge) ferromagnets.[13] Within these MCMs the $(Mn,Fe)_2(P,Si)$-based compounds with a hexagonal crystal structure present an isostructural FOMT with a strong magnetoelastic coupling among the magnetic, structural and electronic degrees of freedom.[5] The system has attracted considerable attention due to advantages such as: rare-earth free, no toxic elements, low cost and a tunable Curie temperature (T_C). To further optimize its GMCE properties, different strategies have been proposed such as tuning the metallic (Fe-Mn) and nonmetallic (P-Si) ratios,[14,15] chemical pressure engineering (substitutional/interstitial doping),[4] nanostructuring,[16] additive manufacturing,[17] etc. As an effective way, alloying with doping elements does not necessarily only tune the T_C, but potentially also change the ΔT_{hys}, which may be detrimental to the cooling/heating efficiency.[18] Most importantly, the GMCE performance is generally degraded.[19–22] Note that benefiting from the co-shared relative low concentration of magnetic atoms (Mn and Fe form 66.7 at% for the model $(Mn,Fe)_2(P,Si)$ alloy), this system has a good potential for the substitution with other elements. To extend its working window for operation, effective ways to simultaneous tune T_C, control a low ΔT_{hys} and maintain the excellent GMCE are still limited, and further optimization methods will be beneficial for producing crucial materials for the design of active magnetic regenerator (AMR) beds, which are based on MCMs.[23,24] Inspired by previous reports about d-block substitutions with the 5d elements W,[25] Ta,[26] and Ru,[27,28] we in this study systematically investigate the influence on MCE properties for 3d Ni, 4d Pd, and 5d Pt (with same valence-electron count) doping to reveal how (micro)structural changes impact the performance, from detailed experiments and theoretical calculations.

In the present study, the independent Ni, Pd and Pt doped $Mn_{1.25}Fe_{0.7-x/y/z}(Ni/Pd/Pt)_{x/y/z}P_{0.5}Si_{0.5}$ materials have successfully been produced and the thermodynamic, GMCE and crystalline structural information has been studied from experimental and theoretical perspectives. It is found that Ni doping degenerates the GMCE, while doping with Pd and Pt can effectively tailor T_C, keep a low ΔT_{hys} (<6 K) and maintain or even enhance the GMCE for a low dopant content ($\lesssim$ 0.04). For example, the maximum $|\Delta s_m|$ of the current Pd and Pt doped materials surpasses almost all other $(Mn,Fe)_2(P,Si)$-based materials with the lowest ΔT_{hys} reported until now. Through X-ray diffraction (XRD), neutron diffraction (ND) experiments, and density functional theory (DFT) calculations, the d-block Ni-Pd-Pt atoms are distinguished as substitutional on the 3f(Fe) sites. The mechanism responsible for the tunable GMCE properties upon different d-block element dopings is understood from the competition between the ferromagnetic exchange interaction and the formation of covalent bonding: for Ni doping the shortened intralayer atomic distances can promote the enhanced d-d and p-d hybridization (relatively modest effect for Pd/Pt), thus leading to a degradation (constant value and even enhancement for Pd/Pt) of GMCE. Our results provide an important understanding on how to control the hybridization degree for d-block elements in various periods, enabling effective ways to tailor the physical properties for an optimal GMCE performance of the $(Mn,Fe)_2(P,Si)$-based MCMs. This may further reinforce its potential for solid-state $M_{CE}EC$ applications.

2. Results and Discussion

The specific heat as a function of temperature (measured by zero-field DSC) for $Mn_{1.25}Fe_{0.7-x}Ni_xP_{0.5}Si_{0.5}$ (x = 0.00, 0.01, 0.02, 0.03, 0.04), $Mn_{1.25}Fe_{0.7-y}Pd_yP_{0.5}Si_{0.5}$ (y = 0.01, 0.02, 0.03, 0.04), and $Mn_{1.25}Fe_{0.7-z}Pt_zP_{0.5}Si_{0.5}$ (z = 0.01, 0.02, 0.03) materials upon heating and cooling is presented in **Figure 1**a–c, respectively. The observed endothermic and exothermic peaks for Ni and Pt doping continuously shift to lower temperatures with an increased dopant content, while for Pd the peaks first increase and then decrease between temperatures ranging from 210 to 270 K. It is worth mentioning that the FOMT could be degraded rapidly for Ni doping because of the reduced specific heat peaks, in comparison to Pd and Pt doping. The corresponding extracted cooling T_C ($T_C^{cooling}$), heating T_C ($T_C^{heating}$), and ΔT_{hys} data for these three doping systems are present in Figure 1d–f. Interestingly, Ni doping reduces ΔT_{hys} from 6.7 to 5.0 K (at a sweep rate of 10 K min^{-1}). However, Pd and Pt doping both enhance ΔT_{hys} to 8.1 and 9.3 K, respectively. This differs with most dopant on this system, which will decrease the ΔT_{hys} (simultaneously degrade the GMCE), excluding the light element F.[29] For $(Mn,Fe)_2(P,Si)$-based materials, the unusual effect of d-block metallic doping on ΔT_{hys} has also been noticed in VB (V-Nb-Ta)[26,30,31] and VIB (Mo-W)[25,32] group doping systems, which could be closely associated with the covalent radius and the electron orbital configurations of these elements. The main thermodynamic parameters extracted from the DSC measurements are summarized in **Table 1**.

The magnetization versus temperature (M–T) curves at an applied field of 1 T for the $Mn_{1.25}Fe_{0.7-x}Ni_xP_{0.5}Si_{0.5}$ (x = 0.00–0.04), $Mn_{1.25}Fe_{0.7-y}Pd_yP_{0.5}Si_{0.5}$ (y = 0.01–0.04), and $Mn_{1.25}Fe_{0.7-z}Pt_zP_{0.5}Si_{0.5}$ (z = 0.01–0.03) materials are shown in **Figure 2**a–c, respectively. A sharp magnetoelastically coupled FOMT from the ferromagnetic state at low temperature to the paramagnetic state at high temperature is observed near room temperature. In this system, the Mn (≈2.5 μ_B) and Fe (≈1.5 μ_B) atoms account for the magnetic moment of the alloy.[33,34] As a similar observation, the shift in T_C observed in the magnetic measurements shows the same trends as found in the DSC

Y. Ren
Center for Neutron Scattering
City University of Hong Kong
Kowloon, Hong Kong SAR 999077, China

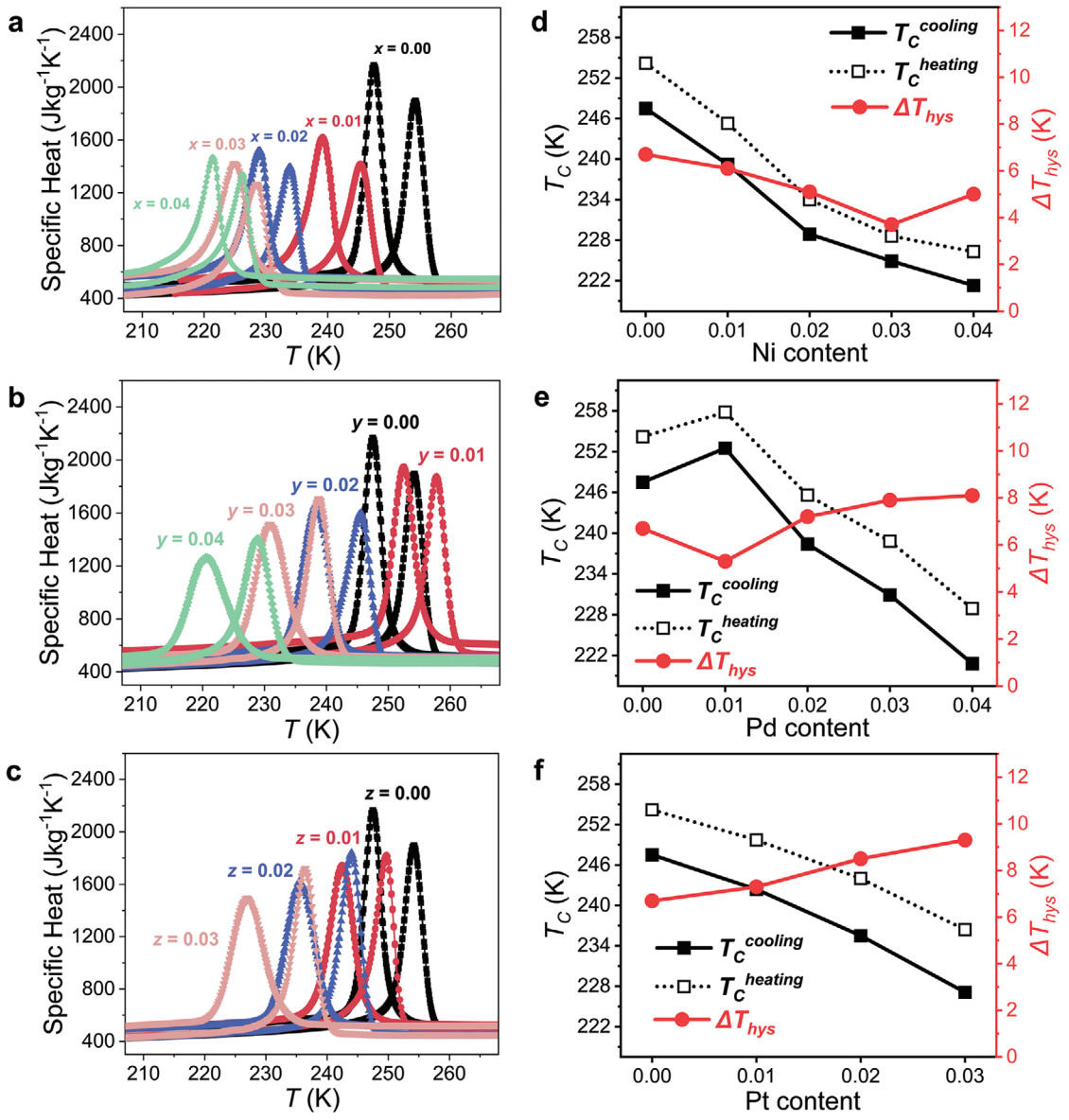

Figure 1. Specific heat derived from DSC experiments for a) $Mn_{1.25}Fe_{0.7-x}Ni_xP_{0.5}Si_{0.5}$ (x = 0.00, 0.01, 0.02, 0.03, 0.04), b) $Mn_{1.25}Fe_{0.7-y}Pd_yP_{0.5}Si_{0.5}$ (y = 0.01, 0.02, 0.03, 0.04), and c) $Mn_{1.25}Fe_{0.7-z}Pt_zP_{0.5}Si_{0.5}$ (z = 0.01, 0.02, 0.03) materials upon heating (right peak) and cooling (left peak). The corresponding extracted $T_C^{cooling}$, $T_C^{heating}$, and ΔT_{hys} as a function of dopant content for (d)–(f).

experiments. Moreover, ignoring the difference in sweep rate (2 K min^{-1} for the SQUID vs 10 K min^{-1} for DSC),[35] the intrinsic values of ΔT_{hys} are all below 6 K. The obtained very low values for ΔT_{hys} are beneficial for the reversibility of the MCE cycles because a large ΔT_{hys} will inevitably degrade the energy efficiency of the AMR under practical conditions.[18] As shown in Figure 2d–f, the magnetization of all samples shows clear saturation at 5 K and 5 T. The inset clearly shows that the total moments have been slightly diluted and the saturation magnetization (M_s) at 5 K has slightly decreased and fluctuates between 145 and 130 A m^2 kg^{-1} as a result of the dopant substitution. It is reasonable that Ni substitution on Fe does not significantly passivate the M_s because of its ferromagnetism nature. However, surprisingly, compared with other nonmagnetic doping elements like V the value of M_s still remains at a high magnitude (>135 A m^2 kg^{-1} starting from 144 A m^2 kg^{-1}) for a limited Pd and Pt content (≤0.03), where V substitution (x = 0.03) reduced M_s from around 154 to 140 A m^2 kg^{-1} in $Mn_{0.97}V_{0.03}Fe_{0.95}P_{0.563}Si_{0.36}B_{0.077}$.[36] As two representatives in platinum-group metal (including Ru, Rh, Ir, Pd, Pt), pure Pd and Pt, which are immediately beneath the "magnetic" Ni, are always recognized as nonmagnetic and have paramagnetic properties.[37] These elements however interact with the strong magnetic elements (e.g., Fe, Co, Ni) and act as an incipient ferromagnet.[37] For example, FeRh materials show a strongly magnetoelastic coupled first-order antiferromagnetic-to-ferromagnetic (AFM-FM) transition, where the Fe moment is around 3.2 μ_B and Rh moment is around 0.9 μ_B.[38] It is possible that Pd and Pt doping in $(Mn,Fe)_2(P,Si)$-based

Table 1. Summary of the values of T_C upon cooling and heating, the thermal hysteresis ΔT_{hys}, the entropy change $|\Delta s_m|$, the magnetization change ΔM and $dT_C/\mu_0 dH$ for $Mn_{1.25}Fe_{0.7-x}Ni_xP_{0.5}Si_{0.5}$ (x = 0.00, 0.01, 0.02, 0.03, 0.04), $Mn_{1.25}Fe_{0.7-y}Pd_yP_{0.5}Si_{0.5}$ (y = 0.01, 0.02, 0.03, 0.04), and $Mn_{1.25}Fe_{0.7-z}Pt_zP_{0.5}Si_{0.5}$ (z = 0.01, 0.02, 0.03) materials, measured by DSC and SQUID.

Sample	Tc^{DSC} (cooling; K)	Tc^{SQUID} (cooling; K)	Tc^{DSC} (heating; K)	Tc^{SQUID} (heating; K)	$\Delta T_{hys}{}^{DSC}$ [K]	$\Delta T_{hys}{}^{SQUID}$ [K]	$\lvert\Delta s_m\rvert$[a] [J kg^{-1} K^{-1}]	ΔM[b] [A m^2 kg^{-1}]	$dT_C/\mu_0 dH$ [K/T]
No dopant	247.5	253.3	254.2	256.2	6.7	2.9	15.2 (23.1)	140	3.9
x = 0.01	239.2	245.7	245.3	247.3	6.1	1.6	10.0 (16.2)	129	3.9
x = 0.02	228.9	235.4	234	236.6	5.1	1.2	11.2 (16.3)	129	3.5
x = 0.03	224.9	229.8	228.6	231.2	3.7	1.4	11.3 (17.2)	127	4.9
x = 0.04	221.3	226.2	226.3	228.4	5	2.2	10.1 (14.8)	127	3.8
y = 0.01	252.5	257.7	257.8	259.2	5.3	1.5	13.5 (20.1)	133	4.9
y = 0.02	238.4	244	245.6	247.2	7.2	3.2	15.0 (23.7)	136	3.9
y = 0.03	230.9	237.7	238.8	241.4	7.9	3.7	16.7 (25.1)	132	2.7
y = 0.04	220.8	227.6	228.9	231.5	8.1	3.9	12.5 (21.5)	131	2.8
z = 0.01	242.4	247.8	249.7	251.2	7.3	3.4	14.8 (20.8)	131	3.9
z = 0.02	235.5	240.3	244	245.5	8.5	5.2	15.0 (23.1)	132	3.6
z = 0.03	227.1	233.3	236.4	238.9	9.3	5.6	13.3 (21.0)	130	3.2

[a] in $\Delta\mu_0 H$ = 1(2) T); [b] from 0.01 to 1 T.

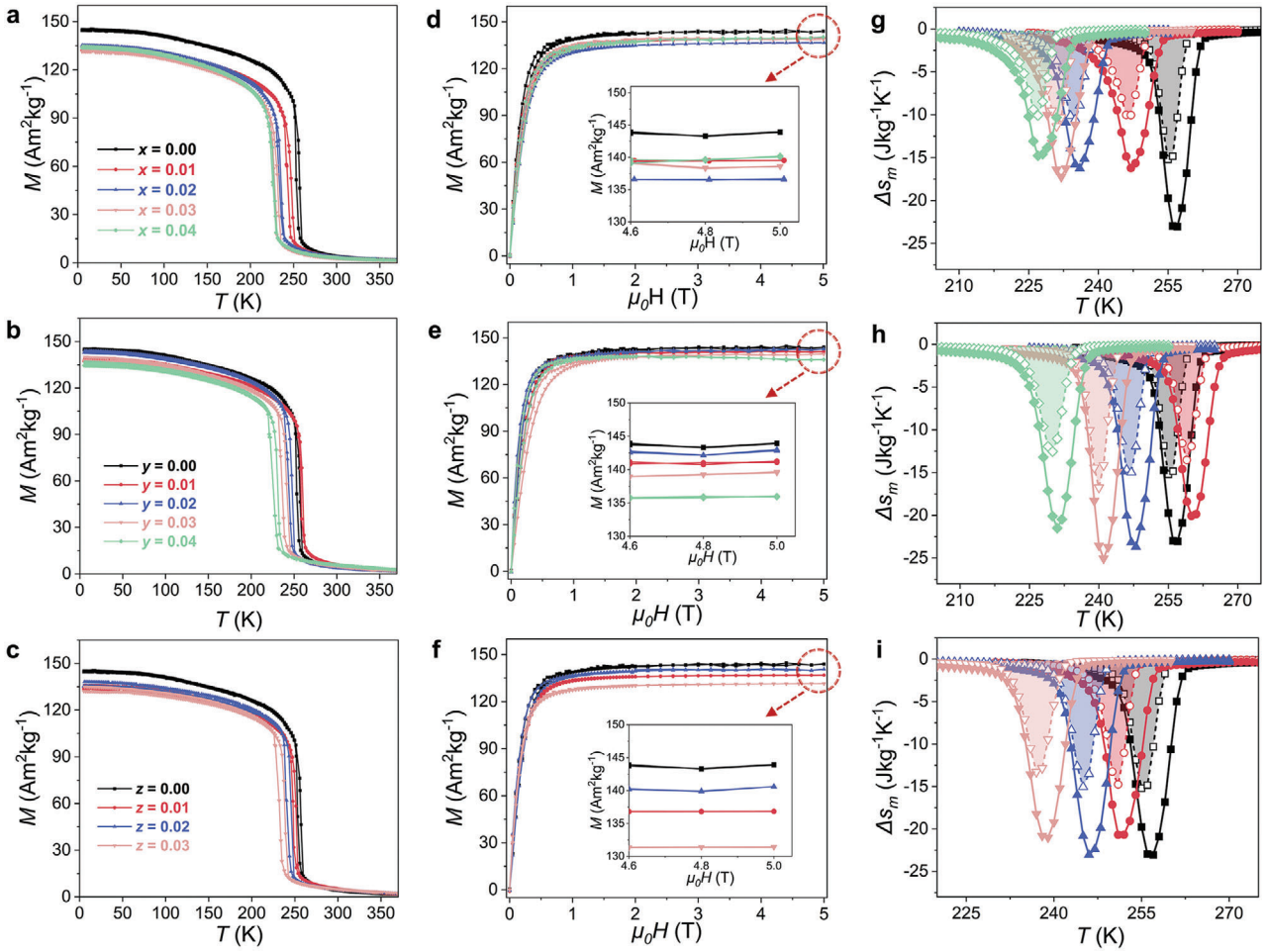

Figure 2. Isofield M–T curves at 1 T for the a) $Mn_{1.25}Fe_{0.7-x}Ni_xP_{0.5}Si_{0.5}$ (x = 0.00, 0.01, 0.02, 0.03, 0.04), b) $Mn_{1.25}Fe_{0.7-y}Pd_yP_{0.5}Si_{0.5}$ (y = 0.01, 0.02, 0.03, 0.04), and c) $Mn_{1.25}Fe_{0.7-z}Pt_zP_{0.5}Si_{0.5}$ (z = 0.01, 0.02, 0.03) alloys. d–f) The corresponding isothermal M–H curves at 5 K for different dopants, respectively. The inset shows the enlarged magnetization changes at high fields. g–i) Δs_m upon heating for $\Delta\mu_0 H$ = 1 T (open symbols) and 2 T (solid symbols) for a varying Ni-Pd-Pt doping contents.

materials behaves similarly. To evaluate the GMCE performance of these compounds in practical Nd-Fe-B permanent magnet field sources (less than 2 T), Figure 2g–i presents the calculated magnetic entropy changes Δs_m (for a magnetic field change $\Delta\mu_0 H$ of 0–2 T) for a varying Ni-Pd-Pt content as a function of the temperature in the vicinity of the FOMT. The value of Δs_m for different field changes $\Delta\mu_0 H$ are calculated using the Maxwell relation by[39]

$$\Delta s_m(T, H) = \int_0^H \left(\frac{\partial M}{\partial T}\right)_H d\mu_0 H \quad (1)$$

The value of $|\Delta s_m|$ remarkably decreases from 23.1 ($x = 0.00$) to 16.2 ($x = 0.01$) J kg^{-1} K^{-1} for $\Delta\mu_0 H = 2$ T (29.9% decrement) for the 3*d* Ni doping, while 4*d* Pd doping can improve the value of $|\Delta s_m|$ to 25.1 ($y = 0.03$) J kg^{-1} K^{-1} (8.7% improvement) and 5*d* Pt doping maintains its excellent $|\Delta s_m|$ at the same field change $\Delta\mu_0 H$. Considering the difference in covalent radius (Ni: 1.24 Å; Pd: 1.39 Å; Pt: 1.36 Å)[40] and the free electron orbital configurations (Ni: [Ar]$3d^8 4s^2$; Pd: [Kr]$4d^{10}$; Pt: [Xe]$4f^{14}5d^9 6s^1$), the competition between covalent bonding and ferromagnetic exchange coupling is expected to be responsible for the difference in magnetic response for these doping elements.[29,32,41] Another key parameter to evaluate the GMCE performance of MCMs is the adiabatic temperature change. By applying the equation $\Delta T_{ad} = \frac{-T}{C_p}\Delta s_m$, where C_p is the specific heat at certain temperature T, the adiabatic temperature change $|\Delta T_{ad}|$ for the representative samples (parent material; $x = 0.01$; $y = 0.03$; $z = 0.02$) is estimated at 3.1, 2.8, 3.5, and 3.1 K for $\Delta\mu_0 H = 2$ T, respectively. The values of T_C, ΔT_{hys}, Δs_m, ΔM, and $dT_C/\mu_0 dH$ obtained from the magnetic measurements have been summarized in Table 1.

For practical applications, the proposed coefficient of refrigeration performance (CRP) defines the suitability of MCMs with hysteresis for cooling/heating applications.[42] The CRP can be expressed as

$$CRP(\mu_0 H_{max}) = \frac{refrigerant\ capacity}{positie\ work\ on\ refrigerant} = \frac{\Delta s \Delta T_{rev}}{\int_0^{\mu_0 H_{max}} M(T_C, \mu_0 H)\, d\mu_0 H} \quad (2)$$

where ΔT_{rev} is the reversible adiabatic temperature change, $\mu_0 H$ the magnetic field, and Δs the entropy change of the system. Therefore, the maximum CRP requires higher Δs. Theoretically, the maximum magnetic entropy change of a material (per mole) corresponds to $R\ln(2J+1)$, with R the universal gas constant and J the total angular momentum.[43,44] The value of Δs_m refers to the total entropy change induced by the applied magnetic field.[45] In **Figure 3**, a performance map of $|\Delta s_m|$ for $\Delta\mu_0 H = 1$ and 2 T as a function of the magnetic transition temperature is presented for the benchmark material Gd and the Fe_2P-type MCMs (with ΔT_{hys} less than 10 K). It is found that the maximum $|\Delta s_m|$ values of Pd/Pt doped samples are about 4–5 times higher than the values for the archetypical MCM Gd of 2.8 (5.2) J kg^{-1} K^{-1} with $\Delta\mu_0 H = 1(2)$ T.[46] It can be seen that the high-performance GMCE is maintained and can be tuned for the doped $Mn_{1.25}Fe_{0.7-y}Pd_yP_{0.5}Si_{0.5}$ ($y = 0.01$–0.04)

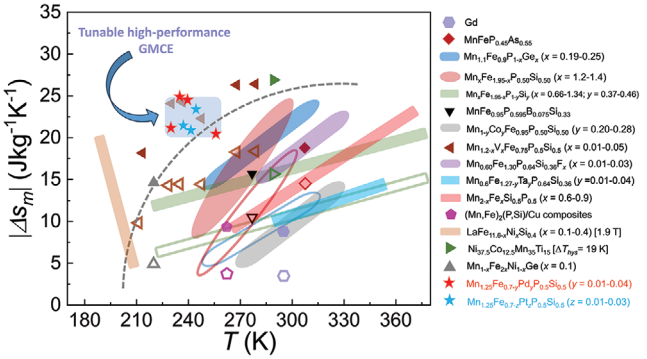

Figure 3. Map of $|\Delta s_m|$ for $\Delta\mu_0 H = 1$ T (open symbols) and 2 T (solid symbols) as a function of the magnetic transition temperature for Gd, Fe_2P-type, typical La(Fe,Si)$_{13}$ based, NiMn-based Heusler and Mn-*M*-*X* based MCMs.[8,19,22,25–27,29,31,39,52–58,64–66] Note that all the selected Fe_2P-type MCMs have a ΔT_{hys} less than 10 K. The stars correspond to the present data for the Pd and Pt doped samples at $\Delta\mu_0 H = 2$ T.

and $Mn_{1.25}Fe_{0.7-z}Pt_zP_{0.5}Si_{0.5}$ ($z = 0.01$–0.03) materials. However, other modification strategies for (Mn,Fe)$_2$(P,Si)-based materials, such as compositional tuning among metallic and non-metallic elements,[14,39] substitutional/interstitial doping with some 3*d*/4*d* transition metals[22,30–32,47,48] or light elements,[29,49–51] dual-phase composites,[52] etc., are always confronted with difficulties like an obvious reduction in $|\Delta s_m|$. It is clearly observed that the maximum $|\Delta s_m|$ of the current Pd and Pt doped materials surpass almost all other (Mn,Fe)$_2$(P,Si)-based materials with a low ΔT_{hys} (<10 K) reported until now,[8,19,22,25–27,29,31,39,52–58] and are also very competitive with other MCMs, like La(Fe,Si)$_{13}$-based materials.[59,60] A comparison of the values of T_C and $|\Delta s_m|$ for different field changes $\Delta\mu_0 H$ in Gd, different Fe_2P-type, typical La(Fe,Si)$_{13}$ based, NiMn-based Heusler and Mn-*M*-*X* based material systems has been presented in **Table 2**. In addition, as shown in Figure S1 (Supporting Information), for the selected no dopant, $x = 0.03$, $y = 0.03$, and $z = 0.02$ samples, the magnetic hysteresis of samples from the isothermal *M*–*H* curves has been determined as 0.8, 0.5, 1.0, and 0.9 T, respectively. The changes in magnetic hysteresis upon doping are in agreement with the trends for ΔT_{hys}. The hysteresis loss is determined by the enclosed area in a field cycle during phase transition. In addition, based on the temperature dependent Δs_m, the refrigeration capacity (*RC*) under the $\Delta\mu_0 H$ of 2 T is evaluated by $RC = \int_{T_c}^{T_h} \Delta s_m\, dT$, where T_h and T_c represent the temperature for the full width at half maximum of the Δs_m curve.[61] Consequently, the reversible *RC* for different samples can be estimated after deducting the maximal hysteresis loss by *RC* under the $\Delta\mu_0 H$ of 2 T.[62] As present in Table S1 (Supporting Information), it is found that the good reversible *RC* of parent sample can be well maintained or improved after Ni, Pd, and Pt doping, because of the reduced hysteresis for Ni doping and the excellent Δs_m for Pd/Pt doping. It is worth noting that the reversible *RC* values for $y = 0.03$ (100.35 J kg^{-1}) and $z = 0.02$ (106.00 J kg^{-1}) under $\Delta\mu_0 H = 2$ T are even better than the $(La_{1-x}Ce_x)_2Fe_{11}Si_2H_y$ ($x = 0.4$) sample (89.4 J kg^{-1}) with negligible magnetic hysteresis,[62] which will be favor of the practical MCE refrigeration applications. For the FOMT it evolves as a nucleation and growth process.[18] The large lattice mismatch

Table 2. Comparison among Gd and different Fe_2P-type material systems reported in the literature for the T_C and $|\Delta s_m|$ for different field changes $\Delta\mu_0 H$ (1 and 2 T).

Material system	T_C [K]	$\lvert\Delta s_m\rvert$ [J kg^{-1} K^{-1}]	Refs.
Gd	≈293	4 (1T); 8.4 (2T)	[8]
$MnFeP_{0.45}As_{0.55}$	≈310	14 (1T); 18 (2T)	[8]
$Mn_{1.1}Fe_{0.9}P_{1-x}Ge_x$ (x = 0.19–0.25)	≈250–330	5–12 (1T); 13–24 (2T)	[53]
$Mn_xFe_{1.95-x}P_{0.50}Si_{0.50}$ (x = 1.2–1.4)	≈245–300	2–16 (1T); 7–25 (2T)	[54]
$Mn_xFe_{1.95-x}P_{1-y}Si_y$ (x = 0.66–1.34; y = 0.37–0.46)	≈220–380	6–12.5 (1T); 12.5–18 (2T)	[39]
$MnFe_{0.95}P_{0.595}B_{0.075}Si_{0.33}$	≈280	10 (1T); 15 (2T)	[19]
$Mn_{1-y}Co_yFe_{0.95}P_{0.50}Si_{0.50}$ (y = 0.20–0.28)	≈270–330	5–13 (2T)	[22]
$Mn_{1.2-x}V_xFe_{0.75}P_{0.5}Si_{0.5}$ (x = 0.01–0.05)	≈210–260	10–15 (1T); 17–27 (2T)	[55]
$Mn_{0.60}Fe_{1.30}P_{0.64}Si_{0.36}F_x$ (x = 0.01–0.03)	≈280–340	9–12 (1T); 15–22 (2T)	[29]
$Mn_{0.6}Fe_{1.27-x}W_xP_{0.64}Si_{0.36}$ (x = 0.01–0.05)	≈260–330	3–7 (1T); 5–12 (2T)	[25]
$Mn_{0.6}Fe_{1.27-y}Ta_yP_{0.64}Si_{0.36}$ (y = 0.01–0.04)	≈290–350	5.5–8 (1T); 10–14 (2T)	[26]
$(Mn,Fe)_2(P,Si)$-based	≈250–280	10–20 (2T)	[56]
$Mn_{2-x}Fe_xSi_{0.5}P_{0.5}$ (x = 0.6–0.9)	≈267–370	7.6–23.0 (2T)	[57]
$Mn_{1.1}Fe_{0.85-x}Nb_xP_{0.43}Si_{0.57}$ (x = 0.01–0.04)	≈255–300	6–10 (1T); 8–14 (2T)	[31]
$(Mn,Fe)_2(P,Si)$/Cu magnetocaloric composites	≈262	4 (1T); 8 (2T)	[52]
$(Mn,Fe,Ru)_2(P,Ge/Si)$-based	≈270–320	6–8 (1T); 12–16 (2T)	[27]
$(Mn,Fe)_2(P,Ge)$Al-based	≈260–290	5–11 (1T); 14–20 (2T)	[58]
$LaFe_{11.6-x}Ni_xSi_{0.4}$ (x = 0.1–0.4)	≈193–214	20-4 (1.9T)	[64]
$Ni_{37.5}Co_{12.5}Mn_{35}Ti_{15}$	≈290	15 (1T); 27 (2T)	[65]
$Mn_{1-x}Fe_{2x}Ni_{1-x}Ge$ (x = 0.1)	≈219	5 (1T); 15 (2T)	[66]

between the ferromagnetic (FM) and paramagnetic (PM) phases can induce considerable elastic strains inside the material, which will further enhance the energy barrier for nucleation and hence increase the thermal/magnetic hysteresis of the magnetoelastic transition.[18,32,62] For the hexagonal $(Mn,Fe)_2(P,Si)$ compounds, the transition-induced elastic strain energy (U_E) can be expressed as $U_E = (C_{11} + C_{12})\, e_1^2 + 2C_{13}e_1e_3 + \frac{1}{2}C_{33}e_3^2$, where the C_{ij} are the elastic constants and e_{ij} are the elastic strain parameters.[29,63] The strain parameters are closely related to $\Delta a/a$ and $\Delta c/c$, which are larger for the FOMT with increased hysteresis.[29] And it was observed an almost linear relationship between the U_E and the ΔT_{hys} for this material system.[32] Therefore, for the current cases, the decreased thermal/magnetic hysteresis for Ni doping and the slight increased hysteresis for Pd/Pt doping could be ascribed to the changes in U_E.

In addition, to distinguish the FOMT with a small ΔT_{hys} from the second order magnetic transition (SOMT) without thermal hysteresis the recently proposed field exponent n for the magnetic entropy change is applied.[67] This field exponent n can be expressed as[67,68]

$$n(T,H) = \frac{dln(|\Delta s_m|)}{dln(H)} \tag{3}$$

The field exponent n as a function of temperature at a mediate field value of 1.4 T has been shown in **Figure 4** for the $Mn_{1.25}Fe_{0.7}P_{0.5}Si_{0.5}$, $Mn_{1.25}Fe_{0.69}Ni_{0.01}P_{0.5}Si_{0.5}$, $Mn_{1.25}Fe_{0.67}Pd_{0.03}P_{0.5}Si_{0.5}$, and $Mn_{1.25}Fe_{0.68}Pt_{0.02}P_{0.5}Si_{0.5}$ samples. It is observed that the exponent n stabilizes at around 1 when the temperature is well below T_C due to the expected field dependence of the magnetization,[69,70] while the n values will abruptly overshoot and finally tends to a value near 2 well above T_C.[36] Note that close to the magnetic transition the n value peaks at a value above the value obtained for the PM state at higher temperature, a characteristic feature for a FOMT.[69,70] Therefore, it is concluded that all samples demonstrate a FOMT, which is in line with the observed latent heat. The significant degradation of $|\Delta s_m|$ in Ni-doped samples implies that for Ni

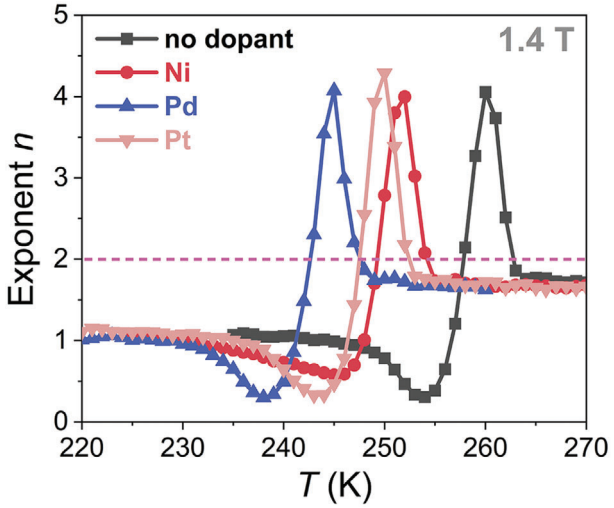

Figure 4. Temperature dependence of the exponent n for $Mn_{1.25}Fe_{0.7}P_{0.5}Si_{0.5}$, $Mn_{1.25}Fe_{0.69}Ni_{0.01}P_{0.5}Si_{0.5}$, $Mn_{1.25}Fe_{0.67}Pd_{0.03}P_{0.5}Si_{0.5}$, and $Mn_{1.25}Fe_{0.68}Pt_{0.02}P_{0.5}Si_{0.5}$ in an applied field of 1.4 T.

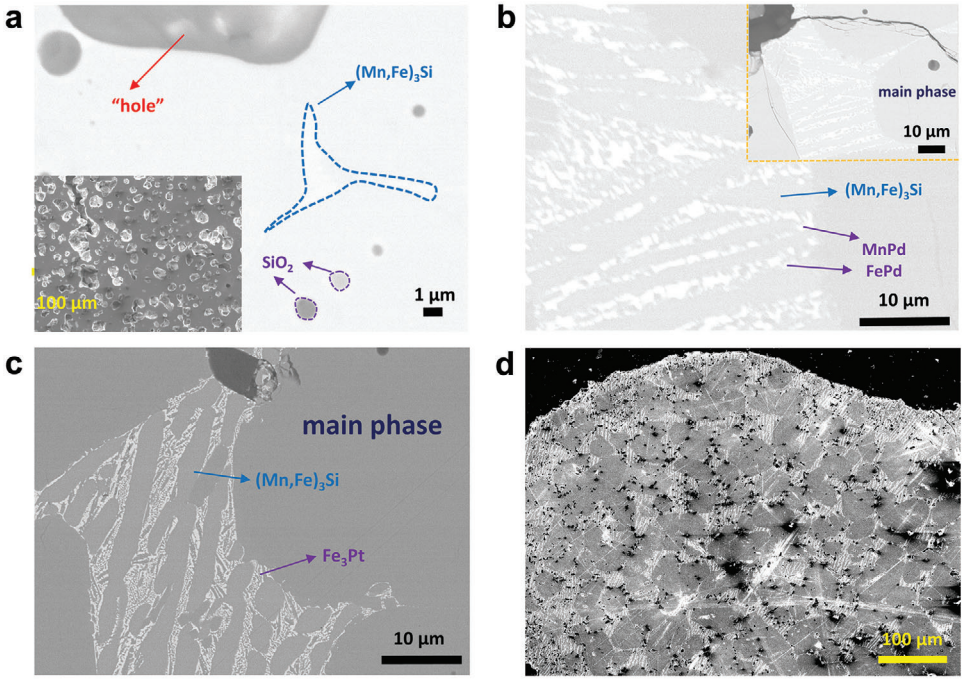

Figure 5. a) Backscattered SEM image for the $x = 0.04$ alloy. The inset shows its morphology. b) Backscattered SEM image for the $y = 0.04$ alloy. The inset shows the distribution of main phase and impurity phases. c) Backscattered SEM image for the $z = 0.03$ alloy at the same magnification as (b). d) Secondary-electron SEM image for the $z = 0.03$ alloy.

system the robust magnetoelastic coupling might be modified in contrast with the Pd and Pt doped systems.[71]

To further investigate the mechanism controlling the effect of Ni/Pd/Pt doping, information about the microstructural changes has been acquired from the SEM measurements, as demonstrated in **Figure 5**. In Figure 5a, only a limited amount of the $(Mn,Fe)_3Si$-based impurity is found for the $Mn_{1.25}Fe_{0.66}Ni_{0.04}P_{0.5}Si_{0.5}$ sample and the EDS analysis determines the compositions as $Mn_{47.5(15)}Fe_{28.8(16)}P_{2.7(2)}Si_{19.4(6)}Ni_{1.5(5)}$. Note that a trace amount of SiO_2 originating from the used raw Si powder is found. The morphology present in the inset shows a wide distribution of cracks and holes in the main matrix, in agreement with previous studies.[56,72] In addition, in Figure 5b two other impurities (MnPd and FePd based) have been seen with dendritic structures within the matrix of the $(Mn,Fe)_3Si$ phase. In Figure 5c, similar as in the Pd case, a certain amount of Fe_3Pt based impurity ($Mn_{48(5)}Fe_{22(4)}P_{2(2)}Si_{18(1)}Pt_{10(1)}$) appears within the $(Mn,Fe)_3Si$ phase. Remarkably, all above Pd and Pt-based impurities are preferentially located at the $(Mn,Fe)_3Si$ phase, rather than in the main phase (as proven from larger area observation in Figure 5d), which is different from other previous cases.[25,26,30] The EDS characterization confirm that Pd and Pt doping is introduced in the main phase.

Moreover, especially for the sharp FOMT, subtle lattice changes can have significantly impact on the magnetic transition, e.g., by the alteration of the coordination environment induced by the physical and chemical pressure from the dopant.[29,32,59,73] As indicated in Figure S1 (Supporting Information), the main phase and the different impurities can be characterized from the high-temperature XRD patterns in the PM state. In **Figure 6**a, the extracted c/a changes for Ni, Pd, and Pt doped compounds have been exhibited. The c/a ratio in this hexagonal system has been found to be closely associated with the magnetic exchange interactions, which govern the magnetoelastic coupling.[74] We observed the c/a ratio keeps increasing with increasing doping content. This trend is inversely correlated with the value of T_C in Figure 1d–f, which indicates a decrease in magnetic exchange interaction upon Ni/Pd/Pt doping due to the proportional correlation between T_C and exchange interaction (within the mean field approximation [MFA]).[75] As shown in Figure 6b the Ni substitution on Fe causes a volume contraction, while Pd and Pt lead to lattice expansion. This is expected due to the difference in covalent radius (Fe: 1.32 Å; Ni: 1.24 Å; Pd: 1.39 Å; Pt: 1.36 Å).[40] Interestingly, the 4*d* Pd doped compound more heavily expands than the 5*d* Pt. The volume changes for these three systems clearly suggest that all dopants have successfully enter the main phase, which is consistent with the SEM-EDS results. In addition, based on the refinement, the concentration changes for different impurities have been evaluated in Figure 6c,d. For example, in Figure 6c, for the $(Mn,Fe)_3Si$ phase (*Fm-3m*), the concentration slightly increases with Ni doping and Pt doping, followed by a reduction. It is worth mentioning that Pd substitution causes a decrease in its concentration from about 9.8 to 5.7 wt% and then shows a stabilization. The abnormal T_C shift (toward higher temperature) with Pd doping for $y = 0.01$ is explained by this decrease, because T_C and the concentration of the $(Mn,Fe)_3Si$ phase were found to show an almost linear relationship.[26] Furthermore, as observed in the SEM measurements, an increased content of Pd and Pt produces extra impurities, in the form of MnPd (*P4/mmm*)/FePd (*Fm-3m*) and Pt_3O4 (*Im-3m*)/Fe_3Pt (*Fm-3m*), respectively. It has been found that a limited amount of impurities containing foreign elements will also reduce T_C, as

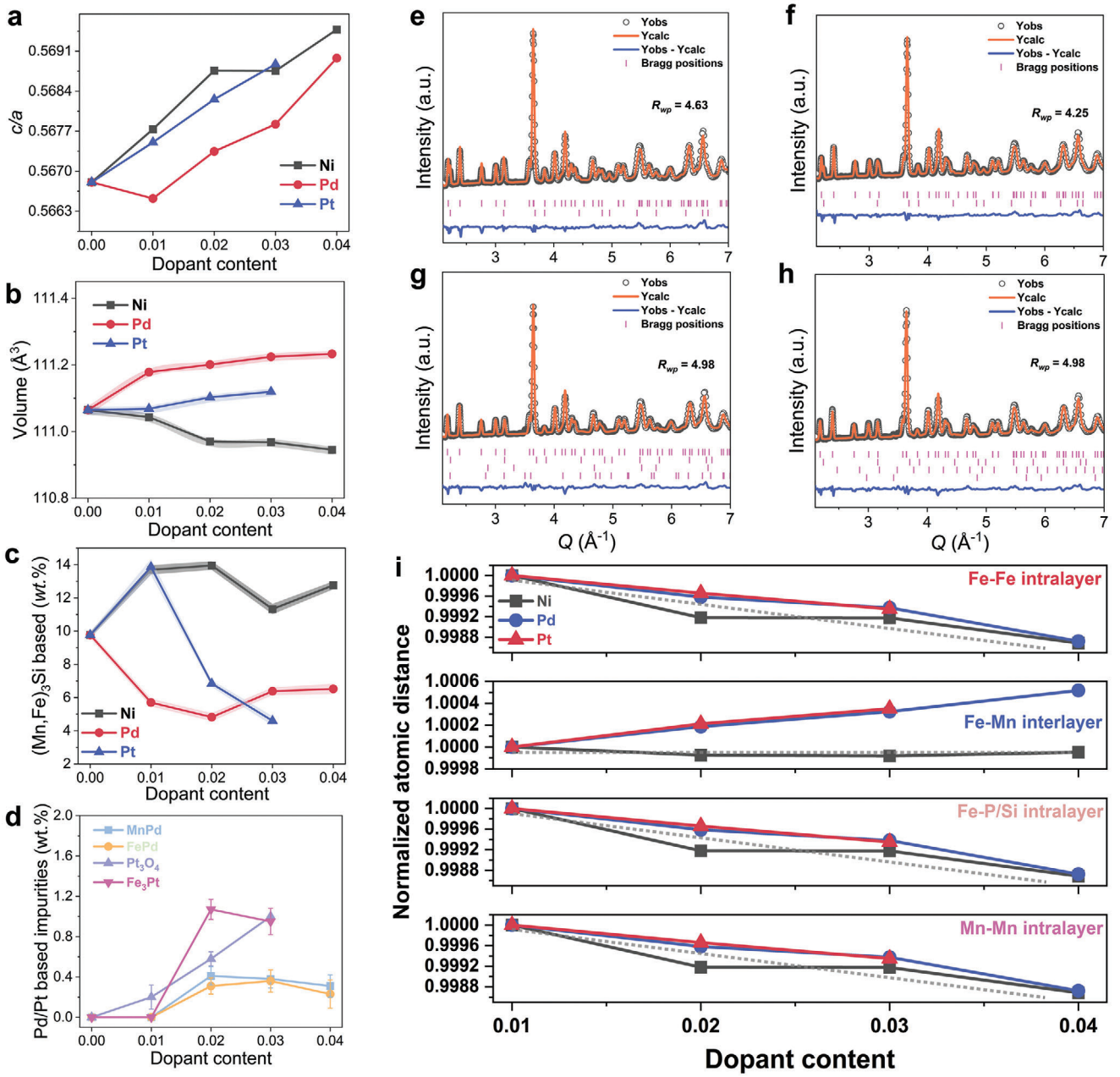

Figure 6. a) *c/a* ratio and b) unit-cell volume *V* as a function of the dopant concentration. Fraction of c) $(Mn,Fe)_3Si$ and d) Pd/Pt based impurity phases for different dopant. (a)–(d) are extracted from high-temperature XRD refinement. Fitted powder neutron diffraction patterns for e) $Mn_{1.25}Fe_{0.7}P_{0.5}Si_{0.5}$, f) $Mn_{1.25}Fe_{0.66}Ni_{0.04}P_{0.5}Si_{0.5}$, g) $Mn_{1.25}Fe_{0.67}Pd_{0.03}P_{0.5}Si_{0.5}$, and h) $Mn_{1.25}Fe_{0.67}Pt_{0.03}P_{0.5}Si_{0.5}$ collected at RT as a function of the wave vector transfer *Q*. Black circles indicate the observed data points, orange lines the calculated profile, blue lines the difference, and vertical lines the Bragg peak positions (top-bottom: a. main phase and $(Mn,Fe)_3Si$ impurity; b. main phase and $(Mn,Fe)_3Si$ impurity; c. main phase, $(Mn,Fe)_3Si$, FePd and MnPd impurities; d. main phase, $(Mn,Fe)_3Si$, Pt_3O_4 and Fe_3Pt impurities). i) Normalized interatomic distances of intralayer Fe-Fe, interlayer Fe-Mn, intralayer Fe-P/Si, and intralayer Mn-Mn as a function of different Ni, Pd, and Pt dopant concentrations for $(Mn,Fe)_2(P,Si)$-based materials.

seen in (Mn,Fe)S,[29] Fe_3W_3C,[25] TaO,[26] etc. In addition, complementary to XRD, ND often possesses a higher sensitivity to light elements and to neighboring elements (e.g., Mn/Fe/Ni/Co). ND has successfully been employed to resolve the occupation of dopants, such as V,[55] Si,[34] Ge,[76] Mo,[32] etc., within the Fe_2P-based lattice structure. Compared with Mn (−3.73 fm) and Fe (9.45 fm), pronounced differences in the coherent neutron scattering length for Ni (10.3 fm), Pd (5.91 fm), and Pt (9.6 fm) enable ND measurements to obtain the pivotal information in precise site occupancy of these metallic dopants. As shown in Figure 6e–h, the good refinement of the ND patterns distinctly distinguish that the preferential site occupancies for Ni/Pd/Pt are 3*f* Fe site rather than 3*f* Mn or 3*g* Mn sites. The χ^2 values of the refinement for different site models can be found in Table S3

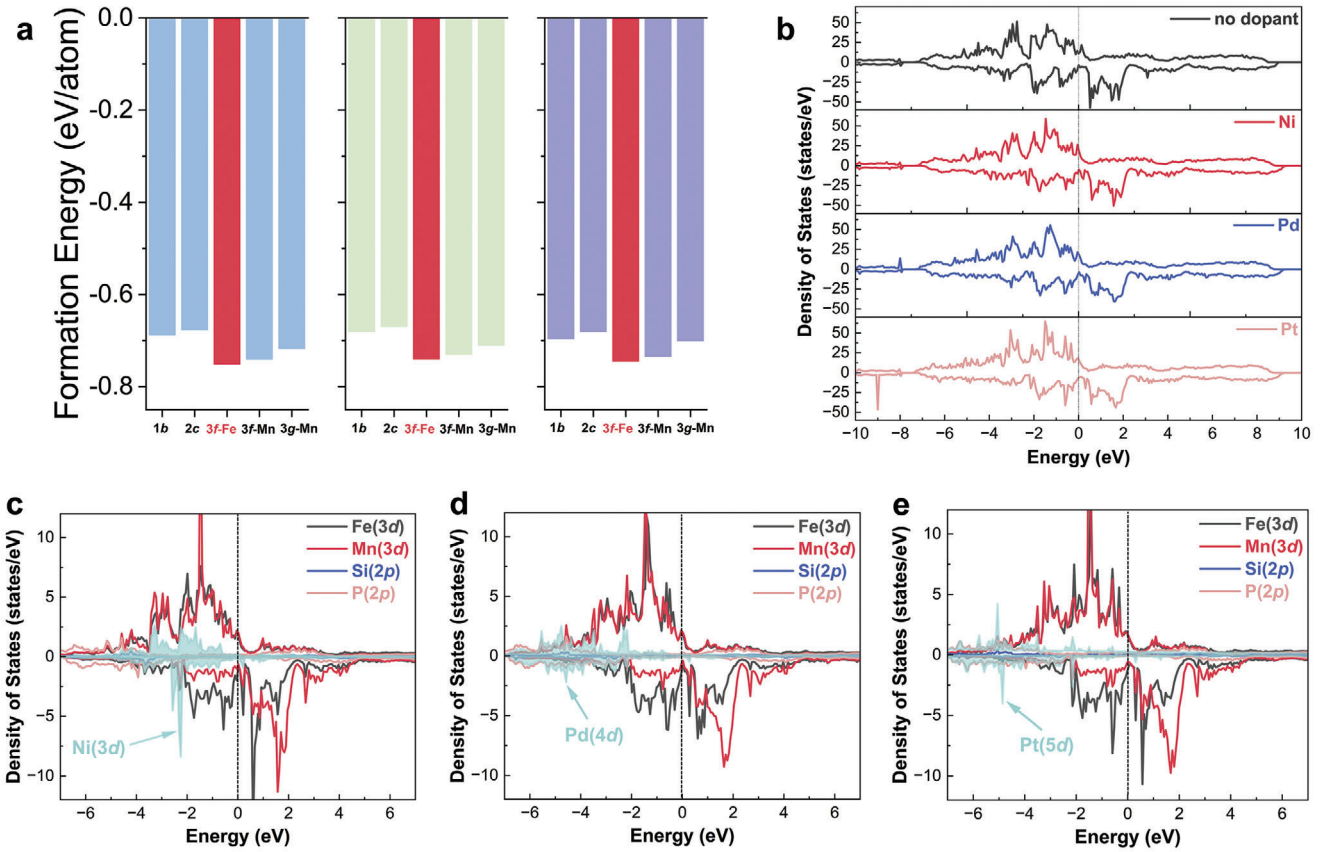

Figure 7. a) Calculated formation energy E_f for different site-occupation models of Ni (left), Pd (middle), and Pt (right) doped $(Mn,Fe)_2(P,Si)$ based materials. b) Total densities of states (DOS) for the no dopant, Ni, Pd, and Pt systems in the FM state. Orbital projected density of states (PDOS) of for c) Ni (3*d*), d) Pd (4*d*), and e) Pt (5*d*) with Mn (3*d*) and Fe (3*d*) in the FM state.

(Supporting Information). Note that the ND results for the Pd and Pt doped alloys are in good agreement with the XRD results. All of structural parameters gained from XRD and ND are summarized in Table S1 (Supporting Information). Based on these structural parameters from the XRD refinement, in Figure 6i the normalized atomic distances among different intralayer and interlayer atom pairs (Fe_{3f}-Fe_{3f}; Fe_{3f}-Mn_{3g}; Fe_{3f}-P/Si_{2c}; Mn_{3g}-Mn_{3g}) have been calculated for all doped samples. With increasing dopant content, for Ni doping the intralayer atomic distances of Fe-Fe, Fe-P/Si, and Mn-Mn significantly decrease (dashed lines), while the reduction for Pd and Pt doping is weaker and almost overlap each other. Nevertheless, for the Fe-Mn interlayer distance there is nearly no change for Ni doping and even a slight rise of about 0.05% for Pd/Pt doping. Recently, systematic ND and XRD studies in similar $(Mn,Fe)_2(P,Ge)$-based alloys elucidated that the changes in the coplanar Fe/Mn–Ge/P bond length have an important influence on T_C and ΔT_{hys}, but that the interplanar length has a limited effect on the magnetocaloric properties.[76] The above experiments reveal that the intralayer distances could be metastable and that the relatively rigid interlayer changes might show a negligible effect on the MCE. Similar results have been reported in the $(Mn,Fe)_2(P,Si)$ series MCMs,[26,29,49] which confirm a strong-correlated relationship between intralayer distances and MCE properties. The exchange interaction among magnetic atoms is responsible for the moment formation and the pattern of magnetic ordering. For the $(Mn,Fe)_2(P,Si)$-based materials the competition between covalent bonding and ferromagnetic exchange coupling is believed to be responsible for the strong GMCE.[29,32,41,73] It was experimentally found that a charge redistribution occurs across the FOMT[41,73] and that doping of F with a very strong electronegativity is found to dramatically modify the bonding properties for this partially localized and itinerant system.[29] From Figure 6i, it can be seen that, especially for Ni doping the shortened intralayer metallic–metallic and metallic–nonmetallic distances dominantly contribute to the strengthened *d–d* hybridization among metallic–metallic pairs and *p-d* hybridization among metallic–metalloid pairs because of the improved electron orbital overlap.[77] This effect may further compromise the impact from the weakened magnetic exchange interactions among magnetic atoms. Consequently, the GMCE properties upon 3*d* Ni substitution are weakened, while the large GMCE maintains after 4*d* Pd and 5*d* Pt doping due to the relatively modest bonding nature.

To provide more insight, we use DFT to calculate the formation energy and density of state (DOS) for different doping systems. First, in **Figure** 7a, the calculated formation energy E_f for different site-occupation models further proves that Ni/Pd/Pt atoms prefer to substitute the 3*f* Fe sites, which is consistent with the ND results. Second, as shown in Figure 7b, the materials exhibit metallic characteristics in the FM state due to the presence of

states at the Fermi level (E_{Fermi}). There is a clear spin splitting between the majority and minority spin channels in the total density of states (TDOS) as the result of exchange splitting. Compared with the undoped parent compound, the E_{Fermi} of Ni, Pd, or Pt doped systems shifts rightward due to the increase of the number of valence electrons, resulting in a mild modification of the TDOS near the E_{Fermi} whose value changes from a local minimum to a local peak that may imply a potential change in the magnetic moments. Surprisingly, the TDOS calculation yields a net saturation magnetic moment of 4.07 (no dopant), 4.08 (Ni), and 4.13 (Pd, Pt) μ_B/*f.u.*, which implies that there is no significant moment modification after substitution. Based on the Stoner model for band magnetism, the reason could be that a limited amount of Ni/Pd/Pt does not aggravate the exchange splitting of the energy bands[78] and has a modest effect on the moment reduction.[79] Moreover, the orbital projected density of states (PDOS) for Ni (3*d*), Pd (4*d*), and Pt (5*d*) with their nearest neighbouring Fe, Mn, P, and Si atoms have been presented in Figure 7c–e. Note that the 4*s* and 6*s* orbitals for Ni and Pt are neglected because of the limited contribution. On the one hand, below E_{Fermi} the overlap of Mn (3*d*) and Fe (3*d*) peaks around −0.5, −1.1, and −2.0 eV demonstrate the typical *d*-*d* hybridization.[80,81] Significant *d*-*d* hybridization also exists between the doped atoms and Fe/Mn atoms, in which the Ni dopant atom hybridizes with Fe/Mn in a higher and wider energy range and has strongest hybridization peaks in the energies about −1 to −3 eV below the Fermi level. The above results support the hypothesis that Ni has the strongest capacity among these three dopants to hybridize the Mn/Fe atoms, and the hybridization will promote the covalent bonding, which is consistent with previous experimental atomic distance changes.

In addition, the metastability in bonding of metallic–nonmetallic pairs is also pivotal for the magneto-elastic transition.[41] The electron localization function (ELF), on the basis of the valence shell electron pair repulsion theory, has been applied to visualize the nature of the possible chemical covalent bonding.[29,82,83] For example, the 2D ELF contour plots for the no dopant, Ni, Pd, and Pt doping samples, sliced along (001) direction, are shown in **Figure** 8a–d. From the topological analysis of the ELF, from 3*d* Ni to 5*d* Pt a significant electron delocalization around the P(2*c*) atoms (nearest neighbour atom of the doped atoms) is confirmed in comparison with the undoped material. Obviously, compared with Ni, Pd, and Pt atoms can more effectively promote electron delocalization in the surroundings of the P(2*c*) atoms. Furthermore, the line profiles of the ELF values between the intralayer and interlayer nearest-neighbor Fe and P/Si atoms are illustrated in Figure 8e,f, respectively. Note that a higher value of ELF corresponds to form a stronger covalent bonding. It is noteworthy that the intralayer changes in the maximum ELF values are greater in comparison of the interlayer one, e.g., Pt substitution can improve the value about 2.53% for the intralayer Fe-P/Si (only 0.59% for the interlayer). However, interestingly, for Pd substitution the value of intralayer Fe-P/Si does almost not change and the interlayer value gently increase, which could be ascribed to the full filling of electrons on its 4*d* orbital based on Hund's rule. Moreover, compared with the Ni doping even Pt doping has higher possibility to form a covalent bonding between Fe-P/Si, but the strength of bonding becomes weaker because the energy level difference among 3*p* in P/Si, 3*d* in Ni, 4*d* in Pd, and 6*s*/5*d* in Pt after considering the Pauling approximate energy level diagram,[77] as well as the electronegativity difference (Ni-1.7; Pd-2.0; Pt-2.1; P-2.1).[84] The above ELF results theoretically confirm the occurrence of covalent bonding between metallic and nonmetallic atoms. It further emphasizes the interplay between the formation of covalent bonding and the ferromagnetic exchange interaction for different *d*-block element doping (e.g., 3*d*-4*d*-5*d*), which can be utilized to optimize the excellent GMCE performance by regulating the metastability in bonding and atomic distances.

3. Conclusions

In summary, the independent *d*-block Ni, Pd, and Pt doped Mn-rich $(Mn,Fe)_2(P,Si)$-based compounds have been studied in terms of their basic thermodynamic, magnetic, and crystalline structure properties. It is found that Ni doping degenerates the GMCE, while Pd and Pt can effectively tailor T_C, keep a low ΔT_{hys} and maintain or even enhance the GMCE for a low dopant contents. The excellent high-performance GMCE properties have been achieved for the designed Pd and Pt doped materials, where the obtained maximum $|\Delta s_m|$ surpass almost all other $(Mn,Fe)_2(P,Si)$-based materials with a low ΔT_{hys}. Furthermore, the preferential substitutional occupancy of the dopants has been clarified through XRD, ND, and DFT calculations. Simultaneously, the physical mechanism is found to arise from the competition between the ferromagnetic exchange interaction and the formation of covalent bonding. Our results provide an important and general understanding of how to control the degree of hybridization for different *d*-block elements (in various periods) doping in the Fe_2P materials family, enabling effective ways to further tailor the physical properties for an optimal GMCE performance of the $(Mn,Fe)_2(P,Si)$-based MCMs.

4. Experimental Section

The off-stoichiometric bulk $Mn_{1.25}Fe_{0.7-x}Ni_xP_{0.5}Si_{0.5}$ (x = 0.00, 0.01, 0.02, 0.03, 0.04), $Mn_{1.25}Fe_{0.7-y}Pd_yP_{0.5}Si_{0.5}$ (y = 0.01, 0.02, 0.03, 0.04), and $Mn_{1.25}Fe_{0.7-z}Pt_zP_{0.5}Si_{0.5}$ (z = 0.01, 0.02, 0.03) MCMs were synthesized by solid-state chemical reaction.[29] In brief, Mn (99.9%), Fe (99.9%), red-P (99.7%), Si (99.9%), Ni (99.90%), Pd (99.90%), and Pt (>99.90%, fuel cell grade) powders with a total mass of 10 g were mixed and milled for 10 h at 380 rpm. Then the pressed cylindrical tablets were sealed in quartz tubes under 200 mbar Ar atmosphere and annealed for 25 h at 1373 K following with rapidly quenched in cold water. A pre-cooling process in liquid nitrogen is applied to remove the so-called "virgin effect"[85] inside the materials.

Differential scanning calorimetry (DSC) measurements were performed using a commercial TA-Q2000 DSC calorimeter in a rate of 10 K min^{-1}. X-ray diffraction (XRD) patterns in the high-temperature paramagnetic state (T_C + 100 °C) were collected using an Anton Paar TTK450 temperature-tunable sample chamber and a PANalytical X-pert Pro diffractometer with Cu Kα radiation. ND experiments were carried out on the time-of-flight (TOF) powder diffractometer at the BL16 Multi-Physics Instrument (MPI) at the China Spallation Neutron Source (CSNS). More instrumental details can be found in ref.[86]. About 6 g of powder sample was placed into a vanadium can (8 mm diameter) and neutron powder diffraction patterns were collected at room temperature (RT). The XRD and ND patterns were analyzed using Fullprof's implementation of the Rietveld refinement method.[87] Field-dependent magnetization (M–H) and temperature-dependent magnetization (M–T) curves were measured in a superconducting quantum interference device (SQUID, Quantum Design MPMS 5XL) magnetometer. Scanning electron microscopy (SEM)

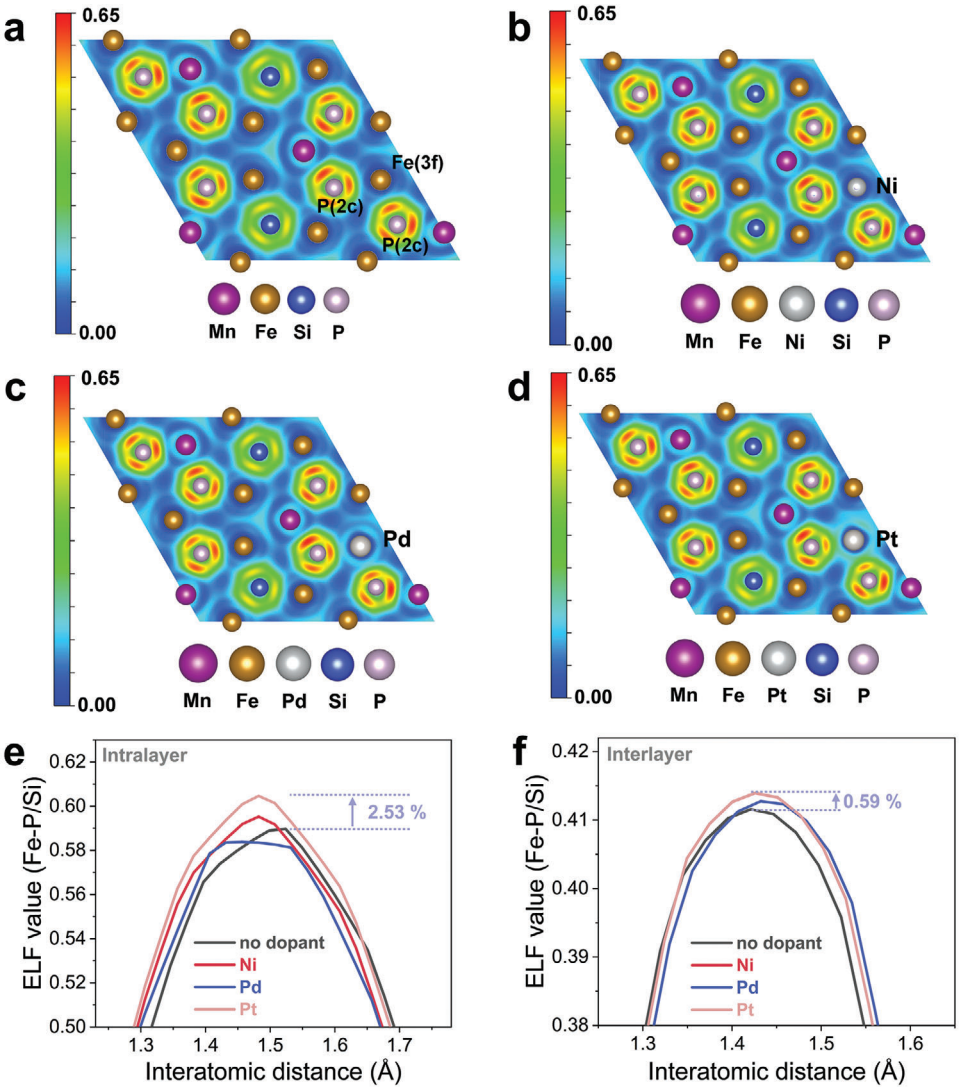

Figure 8. Calculated ELF contour maps for the 3*f* Fe layer with a) no dopant, b) Ni doping, c) Pd doping, and d) Pt doping sliced along (001) direction in the $(Mn,Fe)_2(P,Si)$-based compounds. For different doping systems, line profiles of the ELF values for the e) intralayer Fe-P/Si and f) interlayer Fe-P/Si between Fe and its nearest metalloid neighbors.

was performed on a JSM-7500F field emission SEM equipped with energy-dispersive X-ray spectroscopy (EDS) to study the morphology, microstructure, and composition of samples, and point-scans were used to determine the elemental distribution of different phases.

The calculations are performed in the Vienna ab initio simulation package (VASP) package, in which the plane wave pseudo-potential method and the projector augmented-wave (PAW) pseudopotential with Perdew–Burke–Ernzerhof (PBE) functional are adopted.[88–91] A $2 \times 2 \times 1$ supercell based on a nine-atom unit cell with the composition $Mn_{1.25}Fe_{0.75}P_{0.5}Si_{0.5}$ was used in the calculations. All 3*g* sites were filled by Mn atoms while 3*f* sites were semi-randomly occupied by Fe and Mn atoms. And Si atoms were placed at the 1*b* site and P atoms at the 2*c* site to avoid the high computational cost associated with structural disorder. The plane wave basis cutoff is 500 eV and the thresholds are 10^{-7} eV and 10^{-3} eV Å^{-1} for total energy and force convergence in structural optimization. A mesh of $5 \times 5 \times 15$ *k*-points is used for the structural relaxed, and a mesh of $9 \times 9 \times 31$ *k*-points is used for the electron calculations.

In order to compare the preferred positions of dopant atoms, we calculated the formation energies for all possible sites. The atomic gap sites are disregarded due to the tendency of the larger radius of the dopant atoms to result in structural collapse. Furthermore, experimental results indicate that the gap positions are not susceptible to doping. The formation energy E_{form} is defined by

$$E_{\text{form}} = \frac{1}{36}\left(E_{\text{tot}} - n_1 E_{\text{Fe}} - n_2 E_{Mn} - n_3 E_d - n_4 E_{\text{Si}} - n_5 E_p\right) \quad (4)$$

where E_{tot} and E_d represent the energy of the doped system and the doped atoms, respectively. Parameter n_i is the number of each atom in the supercell. The chemical potential of each atom has been obtained by optimizing the corresponding experimentally synthesized bulk. To investigate the properties of the chemical bonds the ELF[92,93] was conducted. The ELF allows for an accurate characterization of the bonding nature on the basis of the electron densities. The characterization is based on a topological analysis of local quantum-mechanical functions related to the Pauli exclusion principle, where ELF represents the possibility of finding a second electron with the same spin in the vicinity of the reference electron. In

principle, higher ELF values indicate the areas with more localized electrons and show a stronger covalent bonding.

Supporting Information

Supporting Information is available from the Wiley Online Library or from the author.

Acknowledgements

F.Q.Z. greatly appreciates the inspiring discussions with N. van Dijk, E. Brück, and Y. Ren This work was supported by the open research fund of CSNS (Grant Nos. KFKT2022B04 and KFKT2022A05). F.Q.Z. and Y.R. acknowledge financial support from City University of Hong Kong (Project No. 9610533). P.F., F.M., and X.-W.Y. acknowledge financial support from the National Natural Science Foundation of China (Grants Nos. 12074040 and 12274255). F.M. was also supported by the BNU Tang Scholar.

Conflict of Interest

The authors declare no conflict of interest.

Data Availability Statement

The data that support the findings of this study are available from the corresponding author upon reasonable request.

Keywords

d-block element doping, first-order magnetic transition, magnetocaloric energy conversion, magnetocaloric material, Mn-Fe-P-Si

Received: May 29, 2024
Revised: July 23, 2024
Published online:

[1] International Energy Agency, **2018**, Report.
[2] X. Moya, N. D. Mathur, *Science* **2020**, *370*, 797.
[3] A. Kitanovski, *Adv. Energy Mater.* **2020**, *10*, 1903741.
[4] F. Q. Zhang, X. F. Miao, N. van Dijk, E. Brück, Y. Ren, *Adv. Energy Mater.* **2024**, *14*, 2400369.
[5] E. Brück, *J. Phys. D: Appl. Phys.* **2005**, *38*, R381.
[6] K. A. Gschneidner, V. K. Pecharsky, A. O. Tsokol, *Rep. Prog. Phys.* **2005**, *68*, 1479.
[7] V. K. Pecharsky, K. A. Gschneidner, *Phys. Rev. Lett.* **1997**, *78*, 4494.
[8] O. Tegus, E. Brück, K. H. J. Buschow, F. R. de Boer, *Nature* **2002**, *415*, 150.
[9] F. X. Hu, B. G. Shen, J. R. Sun, Z. H. Cheng, G. H. Rao, X. X. Zhang, *Appl. Phys. Lett.* **2001**, *78*, 3675.
[10] A. Planes, L. Manosa, M. Acet, *J. Phys.: Condens. Matter* **2009**, *21*, 233201.
[11] Z. Y. Wei, E. K. Liu, J. H. Chen, Y. Li, G. D. Liu, H. Z. Luo, X. K. Xi, H. W. Zhang, W. H. Wang, G. H. Wu, *Appl. Phys. Lett.* **2015**, *107*, 022406.
[12] A. Chirkova, K. P. Skokov, L. Schultz, N. V. Baranov, O. Gutfleisch, T. G. Woodcock, *Acta Mater.* **2016**, *106*, 15.
[13] L. Caron, N. T. Trung, E. Brück, *Phys. Rev. B* **2011**, *84*, 020414.
[14] N. H. Dung, Ph.D. Thesis, TU Delft **2012**.
[15] X. M. You, M. Maschek, N. H. H. van Dijk, E. Brück, *Entropy* **2022**, *24*, 2.
[16] F. Q. Zhang, C. Taake, B. W. Huang, X. M. You, H. Ojiyed, Q. Shen, I. Dugulan, L. Caron, N. van Dijk, E. Brück, *Acta Mater.* **2022**, *224*, 117532.
[17] X. F. Miao, W. Y. Wang, H. X. Liang, F. J. Qian, M. Q. Cong, Y. J. Zhang, A. Muhammad, Z. J. Tian, F. Xu, *J. Mater. Sci.* **2020**, *55*, 6660.
[18] L. F. Cohen, *Phys. Status Solidi B* **2018**, *255*, 1700317.
[19] F. Guillou, G. Porcari, H. Yibole, N. van Dijk, E. Brück, *Adv. Mater.* **2014**, *26*, 2671.
[20] N. V. Thang, H. Yibole, N. H. van Dijk, E. Brück, *J. Alloys Compd.* **2017**, *699*, 633.
[21] H. Yibole, F. Guillou, L. Zhang, N. H. van Dijk, E. Brück, *J. Phys. D: Appl. Phys.* **2014**, *47*, 075002.
[22] Z. Q. Ou, N. H. Dung, L. Zhang, L. Caron, E. Torun, N. H. van Dijk, O. Tegus, E. Brück, *J. Alloys Compd.* **2018**, *730*, 392.
[23] B. Huang, J. W. Lai, D. C. Zeng, Z. G. Zheng, B. Harrison, A. Oort, N. H. van Dijk, E. Brück, *Int. J. Refrig.* **2019**, *104*, 42.
[24] D. P. Quijano, C. I. Ferreira, E. Brück, *Appl. Therm. Eng.* **2023**, *232*, 120962.
[25] F. Q. Zhang, S. Smits, A. Kiecana, I. Batashev, Q. Shen, N. van Dijk, E. Brück, *J. Alloys Compd.* **2023**, *933*, 167802.
[26] F. Q. Zhang, I. Batashev, N. van Dijk, E. Brück, *Scr. Mater.* **2023**, *226*, 115253.
[27] H. Wada, K. Nakamura, K. Katagiri, T. Ohnishi, K. Yamashita, A. Matsushita, *Jpn. J. Appl. Phys.* **2014**, *53*, 063001.
[28] T. Ohnishi, K. Soejima, K. Yamashita, H. Wada, *Magnetochemistry* **2017**, *3*, 6.
[29] F. Q. Zhang, I. Batashev, Q. Shen, Z. Y. Wu, R. I. Smith, G. A. de Wijs, N. van Dijk, E. Brück, *Acta Mater.* **2022**, *234*, 118057.
[30] J. W. Lai, X. M. You, I. Dugulan, B. W. Huang, J. Liu, M. Maschek, L. van Eijck, N. Dijk, E. Brück, *J. Alloys Compd.* **2020**, *821*, 153451.
[31] S. Y. Hu, X. F. Miao, J. Liu, Z. Q. Ou, M. Q. Cong, O. Haschuluu, Y. Y. Gong, F. J. Qian, Y. R. You, Y. J. Zhang, F. Xu, E. Bruck, *Intermetallics* **2019**, *114*, 106602.
[32] X. F. Miao, Y. Gong, F. Q. Zhang, Y. R. You, L. Caron, F. J. Qian, W. H. Guo, Y. J. Zhang, Y. Y. Gong, F. Xu, N. van Dijk, E. Brück, *J. Mater. Sci. Technol.* **2022**, *103*, 165.
[33] N. H. Dung, L. Zhang, Z. Q. Ou, L. Zhao, L. van Eijck, A. M. Mulders, M. Avdeev, E. Suard, N. H. van Dijk, E. Brück, *Phys. Rev. B* **2012**, *86*, 045134.
[34] X. F. Miao, L. Caron, P. Roy, N. H. Dung, L. Zhang, W. A. Kockelmann, R. A. de Groot, N. H. van Dijk, E. Brück, *Phys. Rev. B* **2014**, *89*, 174429.
[35] O. Gutfleisch, T. Gottschall, M. Fries, D. Benke, I. Radulov, K. P. Skokov, H. Wende, M. Gruner, M. Acet, P. Entel, M. Farle, *Philos. Trans. R. Soc. A* **2016**, *374*, 20150308.
[36] J. W. Lai, X. M. You, J. Law, V. Franco, B. W. Huang, D. Bessas, M. Maschek, D. C. Zeng, N. van Dijk, E. Brück, *J. Alloys Compd.* **2023**, *930*, 167336.
[37] H. J. Albert, L. R. Rubin, in *Platinum Group Metals and Compounds*, Vol. *98*, American Chemical Society, Washington, DC **1971**, Ch. 1, p. 1.
[38] M. E. Gruner, E. Hoffmann, P. Entel, *Phys. Rev. B* **2003**, *67*, 064415.
[39] N. H. Dung, Z. Q. Ou, L. Caron, L. Zhang, D. T. C. Thanh, G. A. de Wijs, R. A. de Groot, K. H. J. Buschow, E. Brück, *Adv. Energy Mater.* **2011**, *1*, 1215.
[40] B. Cordero, V. Gomez, A. E. Platero-Prats, M. Reves, J. Echeverria, E. Cremades, F. Barragan, S. Alvarez, *Dalton Trans.* **2008**, *21*, 2832.
[41] M. F. J. Boeije, P. Roy, F. Guillou, H. Yibole, X. F. Miao, L. Caron, D. Banerjee, N. H. van Dijk, R. A. de Groot, E. Brück, *Chem. Mater.* **2016**, *28*, 4901.
[42] E. Brück, H. Yibole, L. Zhang, *Philos. Trans. R. Soc. A* **2016**, *374*, 20150303.
[43] F. Guillou, H. Yibole, R. Hamane, V. Hardy, Y. B. Sun, J. J. Zhao, Y. Mudryk, V. K. Pecharsky, *Phys. Rev. Mater.* **2020**, *4*, 104402.

[44] J. Cwik, Y. Koshkid'ko, K. Nenkov, A. Mikhailova, M. Malecka, T. Romanova, N. Kolchugina, N. A. de Oliveira, *Phys. Rev. B* **2021**, *103*, 214429.
[45] F. Q. Zhang, Z. Y. Wu, J. L. Wang, W. Y. Chen, Z. D. Wu, x. Chi, C. L. Zhao, S. Eijt, H. Schut, X. D. Bai, Y. Ren, N. van Dijk, E. Brück, *Acta Mater.* **2024**, *234*, 118057.
[46] T. Gottschall, K. P. Skokov, M. Fries, A. Taubel, I. Radulov, F. Scheibel, D. Benke, S. Riegg, O. Gutfleisch, *Adv. Energy Mater.* **2019**, *9*, 1901322.
[47] J. T. Feng, F. J. Qian, D. N. Shi, H. Yang, *Appl. Phys.* **2019**, *9*, 357.
[48] X. F. Miao, *China Patent CN110343934B*, **2019**.
[49] X. F. Miao, N. V. Thang, L. Caron, H. Yibole, R. I. Smith, N. H. van Dijk, E. Brück, *Scr. Mater.* **2016**, *124*, 129.
[50] F. Guillou, H. Yibole, G. Porcari, L. Zhang, N. H. van Dijk, E. Brück, *J. Appl. Phys.* **2014**, *116*, 063903.
[51] N. V. Thang, X. F. Miao, N. H. van Dijk, E. Brück, *J. Alloys Compd.* **2016**, *670*, 123.
[52] X. F. Miao, C. X. Wang, T. W. Liao, S. H. Ju, J. J. Zha, W. Y. Wang, J. Liu, Y. J. Zhang, Q. Y. Ren, F. Xu, L. Caron, *Acta Mater.* **2023**, *242*, 118453.
[53] N. T. Trung, Z. Q. Ou, T. J. Gortenmulder, O. Tegus, K. H. J. Buschow, E. Brück, *Appl. Phys. Lett.* **2009**, *94*, 102513.
[54] N. H. Dung, L. Zhang, Z. Q. Ou, E. Brück, *Appl. Phys. Lett.* **2011**, *99*, 092511.
[55] J. W. Lai, B. W. Huang, X. F. Miao, N. V. Thang, X. M. You, M. Maschek, L. van Eijck, D. C. Zeng, N. van Dijk, E. Brück, *J. Alloys Compd.* **2019**, *803*, 671.
[56] M. Fries, L. Pfeuffer, E. Bruder, T. Gottschall, S. Ener, L. V. S. Diop, T. Gröb, K. P. Skokov, O. Gutfleisch, *Acta Mater.* **2017**, *132*, 222.
[57] A. He, V. Svitlyk, Y. Mozharivskyj, *Inorg. Chem.* **2017**, *56*, 2827.
[58] D. M. Liu, H. Zhang, S. B. Wang, W. Q. Xiao, Z. L. Zhang, N. Tian, C. X. Liu, M. Yue, Q. Z. Huang, J. X. Zhang, J. W. Lynn, *J. Alloys Compd.* **2015**, *633*, 120.
[59] J. W. Lai, H. Sepehri-Amin, X. Tang, J. Li, Y. Matsushita, T. Ohkubo, A. T. Saito, K. Hono, *Acta Mater.* **2021**, *220*, 117286.
[60] K. Imaizumi, A. Fujita, A. Suzuki, M. Kobashi, M. Kato, *Addit. Manuf.* **2024**, *83*, 104076.
[61] J. J. Yang, Z. B. Li, X. L. Zhang, B. Yang, H. L. Yan, D. Y. Cong, X. Zhao, L. Zuo, *Acta Mater.* **2023**, *246*, 118694.
[62] Y. F. Liu, X. Q. Fu, Q. Yu, M. X. Zhang, J. Liu, *Acta Mater.* **2021**, *207*, 116687.
[63] P. Roy, E. Torun, R. A. de Groot, *Phys. Rev. B* **2016**, *93*, 094110.
[64] L. M. Moreno-Ramírez, C. Romero-Muñiz, J. Y. Law, V. Franco, A. Conde, I. A. Radulov, F. Maccari, K. P. Skokov, O. Gutfleisch, *Acta Mater.* **2018**, *160*, 137.
[65] H. N. Bez, A. K. Pathak, A. Biswas, N. Zarkevich, V. Balema, Y. Mudryk, D. D. Johnson, V. K. Pecharsky, *Acta Mater.* **2019**, *173*, 225.
[66] J. Liu, Y. Y. Gong, Y. R. You, X. M. You, B. W. Huang, X. F. Miao, G. Z. Xu, F. Xu, E. Brück, *Acta Mater.* **2019**, *174*, 450.
[67] J. Y. Law, V. Franco, L. M. Moreno-Ramírez, A. Conde, D. Y. Karpenkov, I. Radulov, K. P. Skokov, O. Gutfleisch, *Nat. Commun.* **2018**, *9*, 2680.
[68] T. D. Shen, R. B. Schwarz, J. Y. Coulter, J. D. Thompson, *J. Appl. Phys.* **2002**, *91*, 5240.
[69] V. Franco, J. S. Blázquez, A. Conde, *Appl. Phys. Lett.* **2006**, *89*, 222512.
[70] V. Franco, A. Conde, *Int. J. Refrig.* **2010**, *33*, 465.
[71] J. W. Xu, Z. Wang, H. Huang, Z. L. Li, X. Chi, D. S. Wang, J. Y. Zhang, X. Q. Zheng, J. Shen, W. D. Zhou, Y. Gao, J. W. Cai, T. Y. Zhao, S. G. Wang, Y. Zhang, B. G. Shen, *Adv. Mater.* **2023**, *35*, 2208635.
[72] J. W. Lai, Z. G. Zheng, B. W. Huang, H. Y. Yu, Z. G. Qiu, Y. L. Mao, S. Zhang, F. M. Xiao, D. C. Zeng, K. Goubitz, E. Brück, *J. Alloys Compd.* **2018**, *735*, 2567.
[73] M. Maschek, X. You, M. F. J. Boeije, D. Chernyshov, N. H. van Dijk, E. Brück, *Phys. Rev. B* **2018**, *98*, 224413.
[74] E. K. Delczeg-Czirjak, Z. Gercsi, L. Bergqvist, O. Eriksson, L. Szunyogh, P. Nordblad, B. Johansson, L. Vitos, *Phys. Rev. B* **2012**, *85*, 224435.
[75] M. Meinert, J. M. Schmalhorst, G. Reiss, *J. Phys.: Condens. Matter* **2011**, *23*, 116005.
[76] H. R. Zhang, D. M. Liu, Z. L. Zhang, S. B. Wang, M. Yue, Q. Z. Huang, J. W. Lynn, *J. Appl. Phys.* **2021**, *130*, 133901.
[77] L. Pauling, *General Chemistry*, Courier Corporation, NY **1988**.
[78] B. Fultz, *Phase Transitions in Materials*, Cambridge University Press, Cambridge **2020**.
[79] K. H. J. Buschow, F. R. Boer, *Physics of Magnetism and Magnetic Materials*, Springer, Berlin **2003**.
[80] Y. J. Zhang, W. H. Wang, H. G. Zhang, E. K. Liu, R. S. Ma, G. H. Wu, *Phys. B* **2013**, *420*, 86.
[81] J. Y. Hu, Z. Chen, M. L. Wang, M. Wang, S. G. Wang, G. H. Zheng, X. Liang, W. J. Lu, Y. Q. Ma, *Phys. Rev. B* **2023**, *107*, 094104.
[82] A. Savin, R. Nesper, S. Wengert, T. F. Fassler, *Angew. Chem., Int. Ed.* **1997**, *36*, 1808.
[83] E. K. Liu, W. H. Wang, L. Feng, W. Zhu, G. J. Li, J. L. Chen, H. W. Zhang, G. H. Wu, C. B. Jiang, H. B. Xu, F. de Boer, *Nat. Commun.* **2012**, *3*, 873.
[84] W. Gordy, W. J. O. Thomas, *J. Chem. Phys.* **1956**, *24*, 439.
[85] X. F. Miao, L. Caron, Z. Gercsi, A. Daoud-Aladine, N. H. van Dijk, E. Brück, *Appl. Phys. Lett.* **2015**, *107*, 042403.
[86] J. P. Xu, L. W. Mei, W. Yin, X. L. Wang, W. L. Cai, Z. D. Li, T. Bo, H. C. Chen, B. T. Wang, Y. B. Chen, *Nucl. Instrum. Methods Phys. Res., Sect. A* **2019**, *927*, 161.
[87] H. M. Rietveld, *J. Appl. Crystallogr.* **1969**, *2*, 65.
[88] G. Kresse, J. Furthmuller, *Phys. Rev. B* **1996**, *54*, 11169.
[89] G. Kresse, J. Hafner, *Phys. Rev. B* **1993**, *47*, 558.
[90] P. E. Blochl, *Phys. Rev. B* **1994**, *50*, 17953.
[91] J. P. Perdew, K. Burke, M. Ernzerhof, *Phys. Rev. Lett.* **1996**, *77*, 3865.
[92] X. F. Miao, Y. Gong, L. Caron, Y. R. You, G. Z. Xu, D. Sheptyakov, P. Manuel, F. J. Qian, Y. J. Zhang, F. Xu, N. van Dijk, E. Brück, *Phys. Rev. Mater.* **2020**, *4*, 104407.
[93] J. Liu, Y. R. You, I. Batashev, Y. Y. Gong, X. M. You, B. W. Huang, F. Q. Zhang, X. F. Miao, F. Xu, N. van Dijk, E. Brück, *Phys. Rev. Appl.* **2020**, *13*, 054003.